Journal of Materials Chemistry A

ROYAL SOCIETY OF CHEMISTRY

PAPER

View Article Online
View Journal | View Issue

Cite this: J. Mater. Chem. A, 2025, 13, 17615

Suppressing O-type stacking and cation migration with Mg and Si doping in P2-type Fe–Mn layered oxides for sodium-ion cathodes†

Arup Chakraborty, [a] Robert A. House [ab] and M. Saiful Islam *[ab]

Layered oxide cathodes for Na-ion batteries containing Mn or Fe are of considerable interest for sustainable energy storage applications largely due to cost issues, relative abundance and high capacities. However, these layered cathodes such as $Na_xFe_{0.5}Mn_{0.5}O_2$ exhibit a structural phase transformation (from P2 to O2) at high charge states accompanied by irreversible cation migration into the Na layers and formation of trapped O_2. Here we investigate whether doping into $Na_xFe_{0.5}Mn_{0.5}O_2$ can effectively suppress this phase transformation and cation migration, focusing on the atomic-scale effects of Mg^{2+} and Si^{4+} substitution, using *ab initio* simulation techniques. These dopants are contrasting species in terms of bonding character from divalent ionic (Mg) to tetravalent covalent (Si). Our study indicates that Mg-doping delayed Fe migration into the Na-layers in line with the experiment. In contrast, Si-doping stabilised the P2 phase over the entire charging range and suppresses Fe migration with no O–O dimer formation, suggesting that the Si-doped system should be a promising Na-ion cathode material.

Received 29th January 2025
Accepted 28th April 2025

DOI: 10.1039/d5ta00804b

rsc.li/materials-a

1. Introduction

Na-ion batteries are attracting considerable attention for energy storage applications largely due to the cost advantages and relative abundance of sodium compared to lithium.[1–6] From the several types of Na-ion cathode materials, layered oxide cathodes are of particular interest as they provide high gravimetric capacities.[7–11]

The Fe–Mn-based material, $Na_xFe_{0.5}Mn_{0.5}O_2$, is a promising cathode because of the inexpensive elements and high discharge capacity of ~200 mA h g^{-1}.[12–16] However, this material suffers from a structural phase transition at high voltage (≥4.1 V) linked with the participation of oxide ions in the redox process and capacity fading with cycling. Previous work[12–14,16] investigated the structural properties of $Na_xFe_{0.5}Mn_{0.5}O_2$ including the P2–O2 phase transition at a high charge state accompanied by Fe migration to the O-type Na-ion layers and oxygen redox; the notations P2 and O2 are two different structures in which Na-ions occupy trigonal prismatic (P) and octahedral (O) sites with oxygen stacking of AB···BA and AB···CB, respectively.[17] Cation substitution of some of the transition metal ions (for example, with Mg^{2+} or Ni^{2+}) has been explored to improve capacity retention in $Na_xFe_{0.5}Mn_{0.5}O_2$.[18–22] Recently, efforts have been made to stabilize the P2 phase through a combined approach of Na_2SiO_3 coating and Si^{4+} doping.[23] Studies on related layered oxide cathodes have explored the effects of cation substitution, including Mg^{2+}, Cu^{2+}, Ti^{4+}, and Sb^{5+} dopants.[20,24–36]

It is clear that a key objective is to stabilise the P2 structure of $Na_xFe_{0.5}Mn_{0.5}O_2$ throughout the entire charging process. Prismatic sites in the P-type Na layer are not favourable for transition metal ions to migrate into, so preserving the P2 structure should allow higher capacity and better capacity retention. However, there are limited studies on $Na_xFe_{0.5}Mn_{0.5}O_2$ that have addressed the P2/O2 phase stability range, and the mechanistic features of O-redox and cation migration at the atomic level, which we investigate here using advanced *ab initio* simulation techniques. The atomic-scale effects of partial Mg^{2+} and Si^{4+} substitution on the structural and redox behaviour of $Na_xFe_{0.5}Mn_{0.5}O_2$ are examined; these dopants in the transition metal layers were selected as they are contrasting species in terms of bonding character from divalent ionic (Mg) to tetravalent covalent (Si).

The results indicate that the P2 phase remains stable *versus* O2 up to a high charge state of $x = 0.16$ for Mg-doped $Na_{0.67}Mg_{0.11}Fe_{0.22}Mn_{0.67}O_2$ and up to the top of charge ($x = 0.0$) for Si-doped $Na_{0.67}Si_{0.11}Fe_{0.22}Mn_{0.67}O_2$. At the top of charge, there is cation migration to the Na-layers in both the parent oxide $Na_xFe_{0.5}Mn_{0.5}O_2$ and Mg-doped system, but Fe migration and O–O dimerization are not found in Si-doped $Na_{0.67}Si_{0.11}Fe_{0.22}Mn_{0.67}O_2$.

[a]Department of Materials, University of Oxford, Parks Road, Oxford, OX1 3PH, UK. E-mail: Saiful.islam@materials.ox.ac.uk

[b]The Faraday Institution, Harwell Campus, Didcot, OX11 0RA, UK

† Electronic supplementary information (ESI) available. See DOI: https://doi.org/10.1039/d5ta00804b

2. Results and discussion

2.1. Structural stability of P2/O2 phases at various charge states

The starting point for our phase stability analysis was modelling the P2 structure of $Na_{0.67}Fe_{0.5}Mn_{0.5}O_2$ and $Na_{0.67}Mg_{0.11}Fe_{0.22}Mn_{0.67}O_2$; comparison of the lattice parameters with the available experimental data[16] showed good agreement to within 1.1% (Table 1). One of our main aims was to compare our simulation results with experimental measurements. We therefore used the same composition as in a previous study of Boivin *et al.*[16] on the Mg-doped material in which $Mg_{0.11}$ was considered. Numerous studies on Mg-doped Na_xMO_2 (M = Mg, Ni, Mn *etc.*) materials have shown that Mg typically occupies the transition metal layer.[37,38] In addition, we have not found any experimental studies on Mg substitution at Na sites in Fe–Mn-based layered oxides that we focused on. Therefore, for direct comparison and consistency, we proceeded with the same concentration for the Si-doped material to allow direct comparison between Mg and Si.

There are no experimental reports of the lattice parameters for the Si-doped material $Na_{0.67}Si_{0.11}Fe_{0.22}Mn_{0.67}O_2$; we note that $Na_{0.67}Si_{0.11}Fe_{0.22}Mn_{0.67}O_2$ likely prefers the P2 structure, according to a new concept of cationic potential from Zhao *et al.*[39] (discussed in detail in ESI Note 1†). Nevertheless, Si doping in layered oxide cathodes for Na-ion and Li-ion batteries has been successfully explored.[23,40,41] Therefore, while synthesizing Si-doped layered oxide materials may be possible, it remains challenging. In addition, the formation of all three materials was confirmed from analysis of the phase diagram[42] (Fig. S1 and ESI Note 2†).

As noted, a key objective is to stabilize the P2 structure throughout the entire charging process to allow higher capacity and better capacity retention. We therefore compared the thermodynamic stability of the primary P2 and O2 phases of $Na_xFe_{0.5}Mn_{0.5}O_2$, $Na_xMg_{0.11}Fe_{0.22}Mn_{0.67}O_2$, and $Na_xSi_{0.11}Fe_{0.22}Mn_{0.67}O_2$ (Fig. 1). We calculated the difference in energies, $\Delta E = E(O2) - E(P2)$, for four charge states ($x = 0.67, 0.33, 0.16, 0.00$) as illustrated in Fig. 1c. Here, $E(P2)$ and $E(O2)$ represent the lowest energies of the P2 and O2 structures, respectively, which were taken separately from analysis of more than hundred configurations and the calculated convex hulls (Fig. S2 in ESI†). This approach represents a possible design principle for new P2-type cathode materials in which high capacities can be achieved.

In Fig. 1c, the calculated ΔE between the P2 and O2 phases of undoped and doped $Na_xFe_{0.5}Mn_{0.5}O_2$ at different charge states indicate three main features. First, the P2 phase is stable only in the pristine state ($x = 0.67$) in agreement with experimental observation,[16] whereas the O2 structures are stable at other charge states, namely $x = 0.33$, 0.16, and 0.0. It should be noted that we validated these results for P2/O2 stability of the parent oxide $Na_xFe_{0.5}Mn_{0.5}O_2$ with a range of different density functional theory (DFT) functionals and found the same trend in accord with experiment (Fig. S3 in ESI†). Second, our findings suggest that Mg-doping into $Na_xFe_{0.5}Mn_{0.5}O_2$ extends the P2 phase stability from pristine to $x = 0.16$. Third, Si-doping maintains the P2 structure throughout the entire charging process, from pristine to the top of charge ($x = 0.67$ to 0.0). This result suggests that Si doping would allow a wider charging region, resulting in a higher capacity. Regarding high-valent dopants, recent studies have found Sb^{5+} substitution in a Mn-rich layered oxide cathode suppresses the P2–O2 phase transformation in the high voltage condition.[34] In the following analysis, we explore the underlying reasons for these stability trends.

2.2. Redox activity and oxidation states on charging

To probe redox activities on charging, we examined the oxidation states of the ions in $Na_xFe_{0.5}Mn_{0.5}O_2$, $Na_xMg_{0.11}Fe_{0.22}Mn_{0.67}O_2$, and $Na_xSi_{0.11}Fe_{0.22}Mn_{0.67}O_2$ (using local magnetic moments) as a function of Na content (x) from the pristine material to high charge states ($\geq$0.33), which are shown in Fig. 2. In the pristine state ($x = 0.67$), the Mn-ions in all three materials are found in two oxidation states, Mn^{3+} and Mn^{4+}, and the Fe-ions are consistently in the Fe^{3+} state. Upon charging to $x = 0.33$, all Mn^{3+} ions in $Na_xFe_{0.5}Mn_{0.5}O_2$ and $Na_xMg_{0.11}Fe_{0.22}Mn_{0.67}O_2$ oxidised to Mn^{4+}, while approximately 33% of the Fe^{3+} ions oxidise to Fe^{4+}. Further charging from $x = 0.33$ to $x = 0.0$ leads to oxidation of the remaining Fe^{3+} to Fe^{4+}. These findings on Mn and Fe oxidation states at different charge states align with previous experimental results. XANES studies show that the Mn K-edge shifts to higher energy during initial charging states, followed by the Fe K-edge shift at high charge states in both the undoped parent oxide and Mg-doped material.[16]

In contrast, for $Na_xSi_{0.11}Fe_{0.22}Mn_{0.67}O_2$, the oxidation of Mn^{3+} continues up to $x = 0.16$, followed by oxidation of Fe^{3+}. This extended Mn oxidation at and beyond $x = 0.33$ is due to the

Table 1 Comparison of calculated (using r^{2}SCAN) and experimental[16] lattice parameters of pristine P2-$Na_{0.67}Fe_{0.5}Mn_{0.5}O_2$, $Na_{0.67}Mg_{0.11}Fe_{0.22}Mn_{0.67}O_2$ and $Na_{0.67}Si_{0.11}Fe_{0.22}Mn_{0.67}O_2$

Material	Method	a (Å)	c (Å)	α (°)	β (°)	γ (°)
$Na_{0.67}Fe_{0.5}Mn_{0.5}O_2$	Calc.	2.94	11.12	89.61	90.47	120.84
	Expt.	2.94	11.20	90.00	90.00	120.00
	Δ (%)	0.00	0.70	0.43	0.52	0.70
$Na_{0.67}Mg_{0.11}Fe_{0.22}Mn_{0.67}O_2$	Calc.	2.91	11.06	90.25	90.06	119.33
	Expt.	2.93	11.18	90.00	90.00	120.00
	Δ (%)	0.68	1.07	0.27	0.00	0.55
$Na_{0.67}Si_{0.11}Fe_{0.22}Mn_{0.67}O_2$	Calc.	2.92	11.04	89.98	89.54	119.85

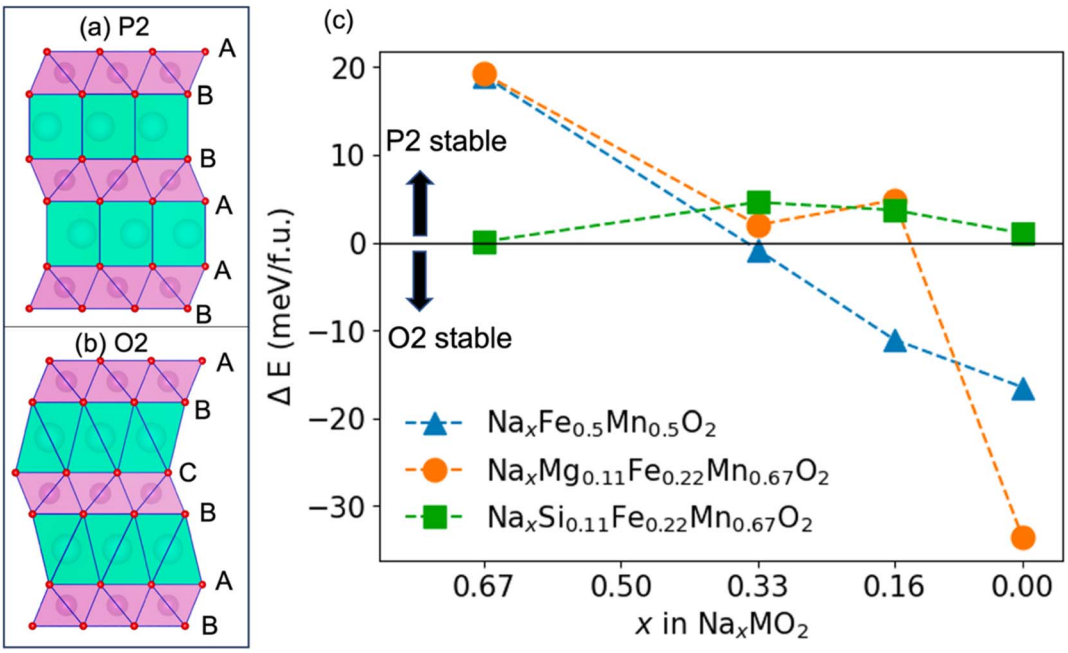

Fig. 1 Schematic representation of (a) P2 and (b) O2 structures, where Na-ions occupy trigonal prismatic (P) and octahedral (O) sites with oxygen stacking of AB···BA and AB···CB, respectively. Atom and polyhedron colour key: Na (green), transition metal (pink) and O (red). (c) Relative energies (ΔE per formula unit) between P2 and O2 structural phases at different charge states of $Na_xFe_{0.5}Mn_{0.5}O_2$, $Na_xMg_{0.11}Fe_{0.22}Mn_{0.67}O_2$, and $Na_xSi_{0.11}Fe_{0.22}Mn_{0.67}O_2$ using PBE + U + D3. The connected lines are guide to the eyes.

presence of high valent Si, which reduces the average Mn oxidation state in the pristine system.

In addition, the simulations indicate O-redox in which localized magnetic moments of 0.1–0.3μ_B exist for certain O ions ($O^{(2-n)-}$), which may be attributed to undercoordinated O-ions. From Fig. 2, there is an enhancement of O-redox at high charge states due to Mg doping. In contrast, there is a general decreasing trend of the number of $O^{(2-n)-}$ ions in both Na_x-$Fe_{0.5}Mn_{0.5}O_2$ and $Na_xSi_{0.11}Fe_{0.22}Mn_{0.67}O_2$.

We also analysed the density of states at various charge states to examine localised states of O ions and to provide clues to the O-redox mechanisms in all three materials (shown in Fig. S4†). The density of states for $Na_xFe_{0.5}Mn_{0.5}O_2$ revealed localised O-p states near the Fermi energy at high charge states which become more pronounced at the top of charge, suggesting that O-ions might participate in the redox process. We found a similar pattern with greater intensity of the localized O-p states near the Fermi energy for $Na_xMg_{0.11}Fe_{0.22}Mn_{0.67}O_2$. In contrast, only weakly localized O-p states appear at the top of charge for $Na_xSi_{0.11}Fe_{0.22}Mn_{0.67}O_2$, which suggests that Si-doping delays or inhibits O-redox participation at high charge states.

2.3. Cation migration and O-dimerization

The nature of oxidised oxygen species and possible formation of O-dimers along with cation migration are critical to understanding the behaviour of these materials at high charge states. To capture kinetic behaviour, we performed *ab initio* molecular dynamics (AIMD) simulations at the top of charge ($x = 0.0$) for the O2 structures of $Na_xFe_{0.5}Mn_{0.5}O_2$, $Na_xMg_{0.11}Fe_{0.22}Mn_{0.67}O_2$, and $Na_xSi_{0.11}Fe_{0.22}Mn_{0.67}O_2$. Here, we considered the lowest energy structures from the previous structural calculations, which typically follow a ribbon-like pattern within the transition metal layers (Fig. S5 in ESI†).

First, considering the parent oxide $Na_xFe_{0.5}Mn_{0.5}O_2$ ($x = 0.0$), the simulations indicate initial Fe ion migration to the Na-layers (Fig. 3a). The mean square displacement (MSD) analysis (Fig. 4) also suggests out-of-plane Fe migration into tetrahedral interstices within the O2-type stacked Na-layers. Boivin *et al.* similarly observed a reduction in the intensity of Fe ions in the transition metal layers in their Fe K-edge EXAFS spectra.[16] Our results also indicate no out-of-plane Mn migration for all three compositions (Fig. 4b). The magnetic moments of the Fe-ions indicate that the migrated Fe ions have an oxidation state of Fe^{3+} which tends to prefer tetrahedral environments. Towards the end of the simulation run, the migrated Fe ions ultimately transitioned from tetrahedral to octahedral coordination (Fig. S6†). We confirmed that these kinetically accessible structures are thermodynamically stable by finding a decrease in total energy (Fig. S7a†) (which used a higher level DFT functional (r^2SCAN)).

For the Mg-doped system, $Na_xMg_{0.11}Fe_{0.22}Mn_{0.67}O_2$, the evolution of the structure along the AIMD trajectory (Fig. 3b) shows that Mg-ions start migrating in the early stages, followed by Fe migration into the Na layers, as shown in the MSD plots (Fig. 4). O-dimers start to form early on and persist throughout the rest of the simulation, with O–O bond distances ranged from 1.30 to 1.48 Å. It is found that the configurations involving Mg and Fe migration followed by O-dimer formation are thermodynamically stable (Fig. S7b†). Such Mg migration and O-

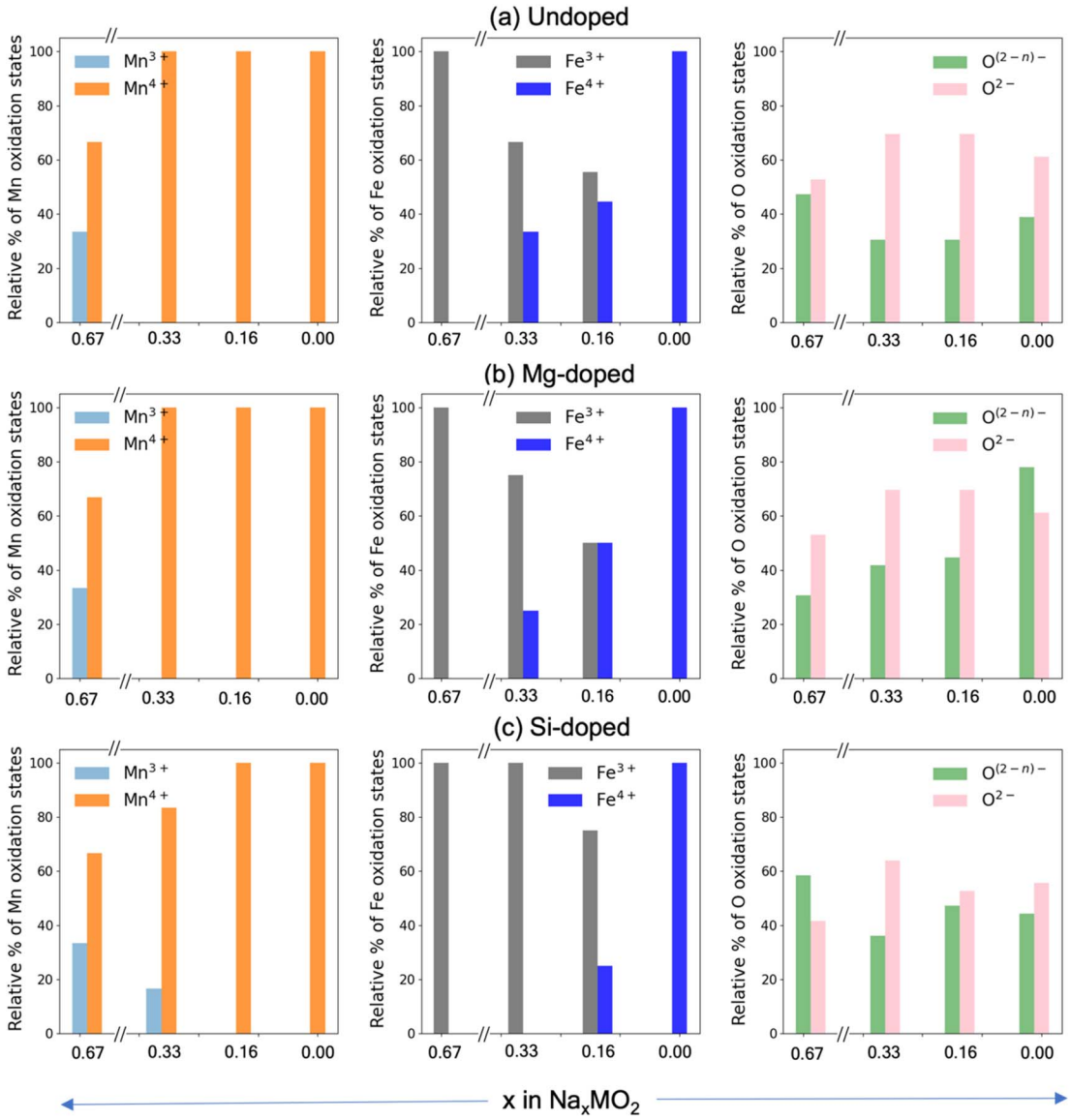

Fig. 2 Redox-active ions in (a) undoped $Na_xFe_{0.5}Mn_{0.5}O_2$, (b) Mg-doped $Na_xMg_{0.11}Fe_{0.22}Mn_{0.67}O_2$, and (c) Si-doped $Na_xSi_{0.11}Fe_{0.22}Mn_{0.67}O_2$ showing the relative % amount of the different oxidation states of Mn, Fe and O as a function of Na content (x) from the pristine material to high charge states ($x = 0.33, 0.16, 0.00$).

redox were also observed from EXAFS and resonance inelastic X-ray spectroscopy (RIXS) measurements, respectively.[16]

The evolution of structures and MSDs for the Si-doped material $Na_xSi_{0.11}Fe_{0.22}Mn_{0.67}O_2$ indicate that, in contrast to the Mg-doped system, there is no out-of-plane migration of either Fe, Mn or Si and no O-dimer formation (Fig. 3c and 4). This result may be related to the strong covalent Si–O bonds, which inhibit the formation of orphan O ions. Consequently, this reduces the likelihood of O-dimer formation or out-of-plane cation migration. Therefore, Si-doping is predicted to be beneficial in stabilizing the P2 structure at high charge states, suggesting that $Na_xSi_{0.11}Fe_{0.22}Mn_{0.67}O_2$ would be a promising P2 cathode material. It is worth noting that in addition to the studies of the low energy ribbon structures, we investigated the effects of honeycomb superstructures (Fig. S8–S10†) and found very similar results on cation migration (detailed in ESI Note 5†).

To further analyse metal–oxygen bond strength (degree of covalency), we calculated the integrated crystal orbital bond index (ICOBI) and the integrated crystal orbital Hamiltonian population (ICOHP) of the metal–O bonds. The Si–O bonds are more robust than Mg–O bonds (Fig. S11†), which indicates that the Si–O bonds are covalent, while Mg–O bond are more ionic in nature. Consequently, these covalent bonds help to stabilise the P2 structure and inhibit cation migration in the Si-doped materials. A recent study showed a similar observation, where covalent Sb–O bonds stabilise the P2 structure in $Na_{2/3}Li_{1/4}Sb_{1/12}Mn_{2/3}O_2$.[43]

Key objectives of our work are to provide design insights and atomistic understanding of Mg and Si doping in P2-type Fe–Mn

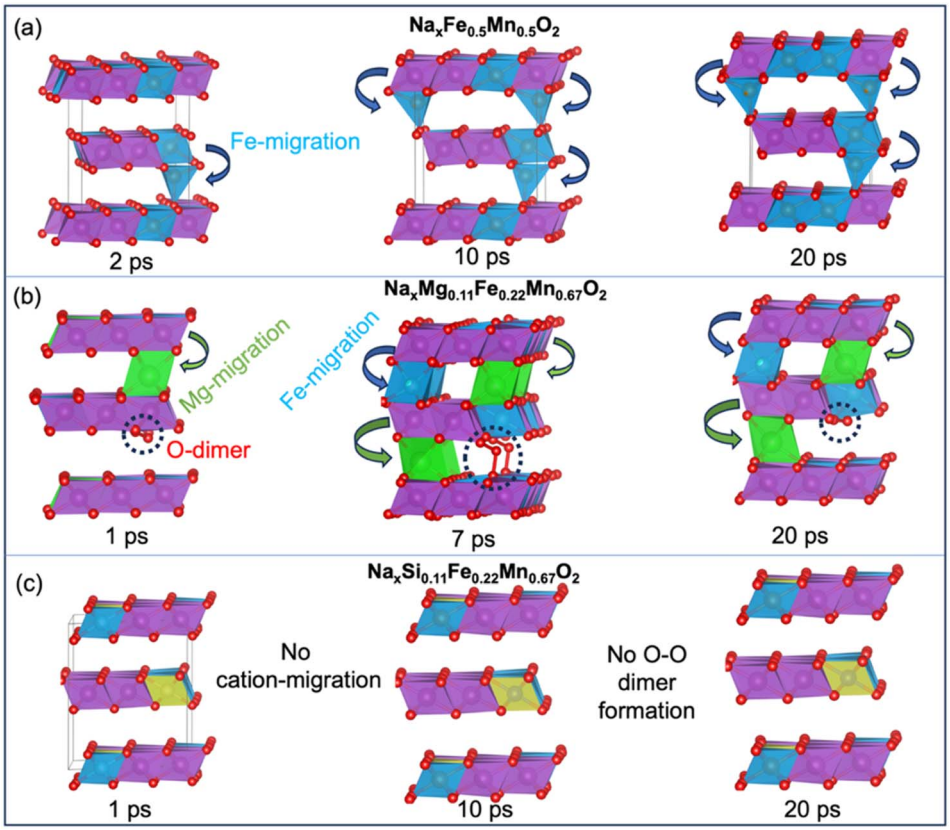

Fig. 3 Evolution of the atomic structures along AIMD trajectories at the top of charge for (a) $Na_xFe_{0.5}Mn_{0.5}O_2$ ($x = 0.0$), showing Fe migration from the octahedral site in the transition metal layer to tetrahedral interstitial sites in the Na-layer, (b) $Na_xMg_{0.11}Fe_{0.22}Mn_{0.67}O_2$ ($x = 0.0$), where Mg first migrates, followed by Fe, from the transition metal layers to the Na-layer. Dotted circles show O-dimer formation; (c) $Na_xSi_{0.11}Fe_{0.22}Mn_{0.67}O_2$ ($x = 0.0$), showing no cation migration. Atom and polyhedron colour key: Mn (purple), Fe (blue), O (red), Mg (green), Si (yellow).

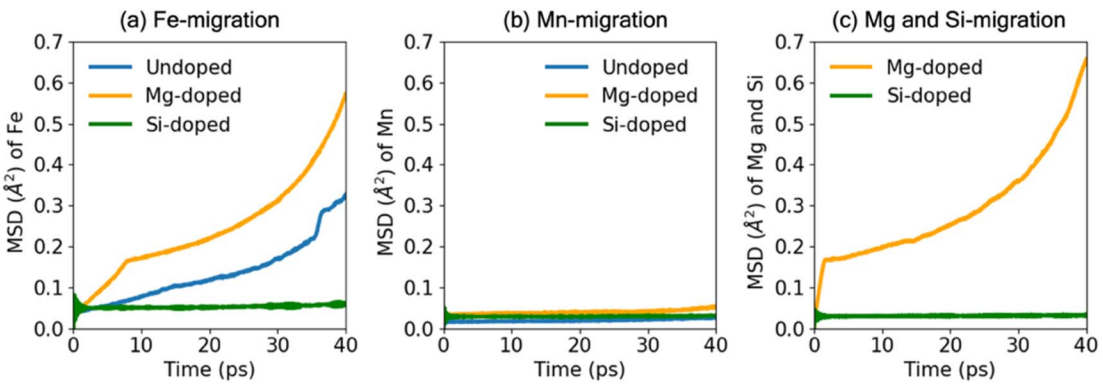

Fig. 4 Mean square displacements (MSD) from AIMD simulations for the out-of-plane migration of (a) Fe, (b) Mn, (c) Mg and Si in undoped ($Na_xFe_{0.5}Mn_{0.5}O_2$), Mg-doped ($Na_xMg_{0.11}Fe_{0.22}Mn_{0.67}O_2$) and Si-doped ($Na_xSi_{0.11}Fe_{0.22}Mn_{0.67}O_2$), at the top of charge ($x = 0.0$).

layered oxides. Such insights are often difficult to obtain by experiment alone. Boivin *et al.* previously synthesized undoped and Mg-doped materials.[16] Preparing Si-doped materials presents experimental challenges using conventional synthesis routes, although prior research has successfully explored Si doping in layered oxide cathodes for both Na-ion and Li-ion batteries.[23,40,41]

3. Conclusions

Our atomic-scale investigation suggests that the Si-doped material, $Na_xSi_{0.11}Fe_{0.22}Mn_{0.67}O_2$, maintains the P2 structure even at the top of charge, which is an important goal for high capacity Na-ion cathodes. The parent oxide P2-type $Na_xFe_{0.5}Mn_{0.5}O_2$ transforms to an O2 structure at $x = 0.33$ in agreement

with experimental observation, and Mg-doping extends the P2 phase stability to $x = 0.16$. Our kinetic study of $Na_xFe_{0.5}Mn_{0.5}O_2$ revealed Fe migration into tetrahedral interstices within the O-type stacked Na-layers, which is consistent with EXAFS experiments. In $Na_xMg_{0.11}Fe_{0.22}Mn_{0.67}O_2$, O-dimers form when Mg ions migrate to the Na layers. In contrast, in $Na_xSi_{0.11}Fe_{0.22}Mn_{0.67}O_2$, we find no migration of Fe, Mn or Si and no O–O dimer formation, indicating that the stronger Si–O covalency can enhance structural stability by strengthening O-binding in the transition metal layers. We recognise possible synthesis challenges for Si substitution, but this study suggests that the Si-doped cathode material should be a promising candidate for Na-ion batteries. Overall, these findings contribute to the broader effort of designing robust P2-type cathode materials.

4. Methods

The DFT calculations were performed using the plane-wave-based Vienna *Ab initio* Simulation Package (VASP) in conjunction with the projector augmented wave (PAW) potential.[44–46] We employed the generalized gradient approximation (GGA), Perdew–Burke–Ernzerhof (PBE) functional with Hubbard-*U* and Grimme's dispersion D3 correction.[47] The effective Hubbard-*U* for Fe and Mn are 4 eV and 5 eV, respectively.[48,49] We have also considered the higher-level *meta*-GGA functional, r^{2}SCAN, to confirm our findings.[50] An energy cut-off of 550 eV and a *k*-mesh of $3 \times 3 \times 2$ were used for all static calculations. The AIMD simulations were also performed with VASP using the PBE + *U* + D3 functional. To speed up our AIMD simulations, we considered an energy cut-off of 400 eV and a single Γ-centered *k*-point.[51] We noted that a larger supercell ($4 \times 3 \times 1$) and an enhanced *k*-mesh ($2 \times 2 \times 2$) also provides similar results (Fig. S12†). Before running the AIMD simulations, we fully optimized the geometries. We initially stabilised the system using NVE ensemble calculations and then selected NVT ensembles employing Nose–Hoover thermostat set at temperatures of $T = 500$ K and 900 K.

Data availability

We have provided data in the main manuscript and the ESI.† Further any data is available from the corresponding author upon reasonable request.

Conflicts of interest

There are no conflicts to declare.

Acknowledgements

A. C. acknowledges the Royal Society Newton International Fellowship grant (NIF\R1\211700) for funding. A. C. and M. S. I. thank the Faraday Institution CATMAT project (EP/S003053/1, FIRG016) for the Michael High-Performance Computing (HPC) facility (FIRG030). This work made use of the UK's National Supercomputer, ARCHER2, through the HEC Materials Chemistry Consortium (EP/R029431). R. A. H. acknowledges the Royal Academy of Engineering for support through the Research Fellowship scheme. We thank Daniel Kwok from Oxford Materials for fruitful discussions.

References

1 N. Yabuuchi, K. Kubota, M. Dahbi and S. Komaba, *Chem. Rev.*, 2014, **114**, 11636–11682.
2 R. Usiskin, Y. Lu, J. Popovic, M. Law, P. Balaya, Y.-S. Hu and J. Maier, *Nat. Rev. Mater.*, 2021, **6**, 1020–1035.
3 N. Tapia-Ruiz, A. R. Armstrong, H. Alptekin, M. A. Amores, H. Au, J. Barker, R. Boston, W. R. Brant, J. M. Brittain, Y. Chen, M. Chhowalla, Y.-S. Choi, S. I. R. Costa, M. Crespo Ribadeneyra, S. A. Cussen, E. J. Cussen, W. I. F. David, A. V. Desai, S. A. M. Dickson, E. I. Eweka, J. D. Forero-Saboya, C. P. Grey, J. M. Griffin, P. Gross, X. Hua, J. T. S. Irvine, P. Johansson, M. O. Jones, M. Karlsmo, E. Kendrick, E. Kim, O. V. Kolosov, Z. Li, S. F. L. Mertens, R. Mogensen, L. Monconduit, R. E. Morris, A. J. Naylor, S. Nikman, C. A. O'Keefe, D. M. C. Ould, R. G. Palgrave, P. Poizot, A. Ponrouch, S. Renault, E. M. Reynolds, A. Rudola, R. Sayers, D. O. Scanlon, S. Sen, V. R. Seymour, B. Silván, M. T. Sougrati, L. Stievano, G. S. Stone, C. I. Thomas, M.-M. Titirici, J. Tong, T. J. Wood, D. S. Wright and R. Younesi, *J. Phys.: Energy*, 2021, **3**, 031503.
4 A. Rudola, A. J. R. Rennie, R. Heap, S. S. Meysami, A. Lowbridge, F. Mazzali, R. Sayers, C. J. Wright and J. Barker, *J. Mater. Chem. A*, 2021, **9**, 8279–8302.
5 D. Kundu, E. Talaie, V. Duffort and L. F. Nazar, *Angew. Chem., Int. Ed.*, 2015, **54**, 3431–3448.
6 E. Goikolea, V. Palomares, S. Wang, I. R. de Larramendi, X. Guo, G. Wang and T. Rojo, *Adv. Energy Mater.*, 2020, **10**, 2002055.
7 W. Zuo, A. Innocenti, M. Zarrabeitia, D. Bresser, Y. Yang and S. Passerini, *Acc. Chem. Res.*, 2023, **56**, 284–296.
8 C. Zhao, Z. Yao, Q. Wang, H. Li, J. Wang, M. Liu, S. Ganapathy, Y. Lu, J. Cabana, B. Li, X. Bai, A. Aspuru-Guzik, M. Wagemaker, L. Chen and Y.-S. Hu, *J. Am. Chem. Soc.*, 2020, **142**, 5742–5750.
9 J. Wang, Y.-F. Zhu, Y. Su, J.-X. Guo, S. Chen, H.-K. Liu, S.-X. Dou, S.-L. Chou and Y. Xiao, *Chem. Soc. Rev.*, 2024, **53**, 4230–4301.
10 M. H. Han, E. Gonzalo, G. Singh and T. Rojo, *Energy Environ. Sci.*, 2015, **8**, 81–102.
11 Z. Chen, Y. Deng, J. Kong, W. Fu, C. Liu, T. Jin and L. Jiao, *Adv. Mater.*, 2024, **36**, 2402008.
12 N. Yabuuchi, M. Kajiyama, J. Iwatate, H. Nishikawa, S. Hitomi, R. Okuyama, R. Usui, Y. Yamada and S. Komaba, *Nat. Mater.*, 2012, **11**, 512–517.
13 E. Talaie, V. Duffort, H. L. Smith, B. Fultz and L. F. Nazar, *Energy Environ. Sci.*, 2015, **8**, 2512–2523.
14 B. Mortemard de Boisse, D. Carlier, M. Guignard, L. Bourgeois and C. Delmas, *Inorg. Chem.*, 2014, **53**, 11197–11205.
15 M. Kim, H. Kim, M. Cho and D. Kim, *J. Mater. Chem. A*, 2021, **9**, 15179–15187.

16 E. Boivin, R. A. House, J.-J. Marie and P. G. Bruce, *Adv. Energy Mater.*, 2022, **12**, 2200702.
17 C. Delmas, C. Fouassier and P. Hagenmuller, *Physica B+C*, 1980, **99**, 81–85.
18 S. Xu, J. Wu, E. Hu, Q. Li, J. Zhang, Y. Wang, E. Stavitski, L. Jiang, X. Rong, X. Yu, W. Yang, X.-Q. Yang, L. Chen and Y.-S. Hu, *J. Mater. Chem. A*, 2018, **6**, 20795–20803.
19 J. W. Somerville, A. Sobkowiak, N. Tapia-Ruiz, J. Billaud, J. G. Lozano, R. A. House, L. C. Gallington, T. Ericsson, L. Häggström, M. R. Roberts, U. Maitra and P. G. Bruce, *Energy Environ. Sci.*, 2019, **12**, 2223–2232.
20 J. W. Somerville, R. A. House, N. Tapia-Ruiz, A. Sobkowiak, S. Ramos, A. V. Chadwick, M. R. Roberts, U. Maitra and P. G. Bruce, *J. Mater. Chem. A*, 2018, **6**, 5271–5275.
21 Q. Shi, R. Qi, X. Feng, J. Wang, Y. Li, Z. Yao, X. Wang, Q. Li, X. Lu, J. Zhang and Y. Zhao, *Nat. Commun.*, 2022, **13**, 3205.
22 F. Fu, X. Liu, X. Fu, H. Chen, L. Huang, J. Fan, J. Le, Q. Wang, W. Yang, Y. Ren, K. Amine, S.-G. Sun and G.-L. Xu, *Nat. Commun.*, 2022, **13**, 2826.
23 J. Jiao, K. Wu, R. Dang, N. Li, X. Deng, X. Liu, Z. Hu and X. Xiao, *Electrochim. Acta*, 2021, **384**, 138362.
24 X. Zhang, W. Zuo, S. Liu, C. Zhao, Q. Li, Y. Gao, X. Liu, D. Xiao, I. Hwang, Y. Ren, C.-J. Sun, Z. Chen, B. Wang, Y. Feng, W. Yang, G.-L. Xu, K. Amine and H. Yu, *Adv. Mater.*, 2024, **36**, 2310659.
25 K. Zhang, Z. Xu, G. Li, R.-J. Luo, C. Ma, Y. Wang, Y.-N. Zhou and Y. Xia, *Adv. Energy Mater.*, 2023, **13**, 2302793.
26 G. Zhang, J. Li, Y. Fan, Y. Liu, P. Zhang, X. Shi, J. Ma, R. Zhang and Y. Huang, *Energy Storage Mater.*, 2022, **51**, 559–567.
27 L. Yang, X. Li, J. Liu, S. Xiong, X. Ma, P. Liu, J. Bai, W. Xu, Y. Tang, Y.-Y. Hu, M. Liu and H. Chen, *J. Am. Chem. Soc.*, 2019, **141**, 6680–6689.
28 X. Wang, Q. Zhang, C. Zhao, H. Li, B. Zhang, G. Zeng, Y. Tang, Z. Huang, I. Hwang, H. Zhang, S. Zhou, Y. Qiu, Y. Xiao, J. Cabana, C.-J. Sun, K. Amine, Y. Sun, Q. Wang, G.-L. Xu, L. Gu, Y. Qiao and S.-G. Sun, *Nat. Energy*, 2024, **9**, 184–196.
29 J.-k. Park, G.-g. Park, H. H. Kwak, S.-T. Hong and J.-w. Lee, *ACS Omega*, 2018, **3**, 361–368.
30 Y. Niu, Z. Hu, B. Zhang, D. Xiao, H. Mao, L. Zhou, F. Ding, Y. Liu, Y. Yang, J. Xu, W. Yin, N. Zhang, Z. Li, X. Yu, H. Hu, Y. Lu, X. Rong, J. Li and Y.-S. Hu, *Adv. Energy Mater.*, 2023, **13**, 2300746.
31 Y. Niu, Z. Hu, H. Mao, L. Zhou, L. Wang, X. Lou, B. Zhang, D. Xiao, Y. Yang, F. Ding, X. Rong, J. Xu, W. Yin, N. Zhang, Z. Li, Y. Lu, B. Hu, J. Lu, J. Li and Y.-S. Hu, *Energy Environ. Sci.*, 2024, **17**, 7958–7968.
32 L. Mu, S. Xu, Y. Li, Y.-S. Hu, H. Li, L. Chen and X. Huang, *Adv. Mater.*, 2015, **27**, 6928–6933.
33 Y. Liu, D. Wang, H. Li, P. Li, Y. Sun, Y. Liu, Y. Liu, B. Zhong, Z. Wu and X. Guo, *J. Mater. Chem. A*, 2022, **10**, 3869–3888.
34 S. Jamil, F. Mudasar, T. Yuan, M. Fasehullah, G. Ali, K. H. Chae, O. Voznyy, Y. Zhan and M. Xu, *ACS Appl. Mater. Interfaces*, 2024, **16**, 14669–14679.
35 H. Hu, C.-W. Kao, C. Cheng, X. Xia, Y. Shen, X. Zhou, G. Liu, L. Wang, P. Zeng, J. Mao, T.-S. Chan and L. Zhang, *ACS Appl. Mater. Interfaces*, 2023, **15**, 30332–30341.
36 Y.-J. Guo, P.-F. Wang, Y.-B. Niu, X.-D. Zhang, Q. Li, X. Yu, M. Fan, W.-P. Chen, Y. Yu, X. Liu, Q. Meng, S. Xin, Y.-X. Yin and Y.-G. Guo, *Nat. Commun.*, 2021, **12**, 5267.
37 G. Singh, N. Tapia-Ruiz, J. M. Lopez del Amo, U. Maitra, J. W. Somerville, A. R. Armstrong, J. Martinez de Ilarduya, T. Rojo and P. G. Bruce, *Chem. Mater.*, 2016, **28**, 5087–5094.
38 Y. Li, K. A. Mazzio, N. Yaqoob, Y. Sun, A. I. Freytag, D. Wong, C. Schulz, V. Baran, A. S. J. Mendez, G. Schuck, M. Zając, P. Kaghazchi and P. Adelhelm, *Adv. Mater.*, 2024, **36**, 2309842.
39 C. Zhao, Q. Wang, Z. Yao, J. Wang, B. Sánchez-Lengeling, F. Ding, X. Qi, Y. Lu, X. Bai, B. Li, H. Li, A. Aspuru-Guzik, X. Huang, C. Delmas, M. Wagemaker, L. Chen and Y.-S. Hu, *Science*, 2020, **370**, 708–711.
40 D.-H. Kim, J.-H. Song, C.-H. Jung, D. Eum, B. Kim, S.-H. Hong and K. Kang, *Adv. Energy Mater.*, 2022, **12**, 2200136.
41 D. Yuan, H. Zhai, Y. Shen, L. Wang, A. Chen and Y. Cheng, *J. Energy Storage*, 2024, **84**, 110944.
42 J. Buckeridge, D. O. Scanlon, A. Walsh and C. R. A. Catlow, *Comput. Phys. Commun.*, 2014, **185**, 330–338.
43 X. Cai, Z. Shadike, N. Wang, X.-L. Li, Y. Wang, Q. Zheng, Y. Zhang, W. Lin, L. Li, L. Chen, S. Shen, E. Hu, Y.-N. Zhou and J. Zhang, *J. Am. Chem. Soc.*, 2025, **147**, 5860–5870.
44 G. Kresse and J. Hafner, *Phys. Rev. B: Condens. Matter Mater. Phys.*, 1993, **47**, 558–561.
45 G. Kresse and J. Furthmüller, *Comput. Mater. Sci.*, 1996, **6**, 15–50.
46 G. Kresse and J. Furthmüller, *Phys. Rev. B: Condens. Matter Mater. Phys.*, 1996, **54**, 11169–11186.
47 S. Grimme, J. Antony, S. Ehrlich and H. Krieg, *J. Chem. Phys.*, 2010, **132**, 154104.
48 D. A. Tompsett, S. C. Parker and M. S. Islam, *J. Am. Chem. Soc.*, 2014, **136**(4), 1418–1426.
49 S. Singh, A. Chakraborty, A. Neveu, P. K. Jha, V. Pralong, M. Fichtner, M. S. Islam and P. Barpanda, *Chem. Mater.*, 2024, **36**(16), 8088–8097.
50 J. W. Furness, A. D. Kaplan, J. Ning, J. P. Perdew and J. Sun, *J. Phys. Chem. Lett.*, 2020, **11**(19), 8208–8215.
51 K. McColl, R. A. House, G. J. Rees, A. G. Squires, S. W. Coles, P. G. Bruce, B. J. Morgan and M. S. Islam, *Nat. Commun.*, 2022, **13**, 5275.